Nonorthogonal wavelet transformation for reconstructing gravitational wave signals

Soumen Roy [*]

Nikhef, Science Park 105, 1098 XG Amsterdam, The Netherlands
and Institute for Gravitational and Subatomic Physics (GRASP), Utrecht University, Princetonplein 1,
3584 CC Utrecht, The Netherlands

Detections of gravitational-wave signals from compact binary coalescences have enabled us to study extreme astrophysical phenomena and explore fundamental physics. A crucial requisite for these studies is to have accurate signal models with characteristic morphologies, which have been challenging for many decades, and researchers are still endeavoring to incorporate important physics. Therefore, morphology-independent methods have been developed for identifying a signal and its reconstruction. The reconstructed signal allows us to test the agreement between the observed signal and the waveform posterior samples from parameter estimation. These methods model observed signals using a nearly orthogonal wavelet basis in the frame of continuous wavelet transformation. Here, we propose log-uniform scales to construct the wavelets, which are are highly redundant (nonorthogonal) compared to the conventional octave scales but more efficient for reconstructing the signals at high frequencies. And we introduce a semi-model-dependent reconstruction method using the posterior samples of the events, where we model the signal using Gabor-Morlet wavelets with log-uniform scales. We demonstrate the ability to detect deviation using a numerical simulation of an eccentric binary black hole merger, where the signal in the data does not belong to the search template waveform manifold. Finally, we apply this method to each binary black hole merger event in GWTC-1. We have found that the signal produced by the GW150914 event has 96% agreement with the waveform posterior samples. As the detector sensitivity improves and the detected population of black hole mergers grows, we expect the proposed method will provide even stronger tests.

I. INTRODUCTION

Detecting gravitational waves (GWs) from the merging compact binaries consisting of black holes and neutron stars has ushered in a new era of observational astronomy [1,2]. So far, the network of Advanced LIGO and Advanced Virgo detectors has observed more than 90 of these events [3–8]. Observations of compact binary mergers allow us to design a range of novel tests of general relativity (GR) in the strong-field regime [9–11]. A current limitation on tests of beyond-GR physics with compact binary coalescences is the lack of understanding of the strong-field merger regime in nearly all modified theories of gravity. Thereby, we generally perform the tests assuming GR to be the null hypothesis or evaluate the consistency of the data with predictions from the theory. At the same time, the latter test can reveal if any unknown binary parameter influences the observed signal.

The continuous wavelet transformation (CWT) based time-frequency analysis has played a crucial role in identifying the gravitational wave events and detecting the deviation from general relativity. Most potential gravitational wave sources, such as compact binary mergers and supernovae explosions, produce nonstationary signals. The CWT is a powerful analysis tool that allows us to obtain a time-frequency localized projection of a nonstationary signal. This procedure calculates the wavelet coefficients by performing a scalar product between the signal and wavelet basis. These coefficients are used not only for time-frequency analysis but also to reconstruct the original time-domain signal. The existing time-frequency-based methods such as coherent wave burst (CWB) [12–14], BAYESWAVE [15,16], and X-pipeline [17,18] are designed for searching unmodeled gravitational-wave bursts and reconstructing the signal from the coherent response of a network of detectors. The previous studies reported satisfactory agreement between the reconstructed signal and the estimated waveform of binary black hole (BBH) mergers for the louder events [3,19,20].

The conventional burst search method identifies a cluster of pixels from the time-frequency map of a detector's strain data if each of those pixels has more power than one expects from the noise alone, called triggers. If the triggers from a network of detectors are coincident, then the method claims a detection of a signal [21]. The CWB method first constructs a multiresolution time-frequency map of the strain data using Wilson-Daubechies-Meyer wavelets [22] and uses the same strategy to detect the events. After that, the method employs a coherent framework of the constrained maximum likelihood approach to yield the event properties: sky location, wave

---

polarization, and signal reconstruction [13,23]. In contrast the BAYESWAVE method employs a framework of Bayesian statistics without relying on any prior assumption of waveform morphology [15]. This method reconstructs the gravitational wave signals and instrumental noise, where both of them are characterized as a superposition of Gabor-Morlet wavelets or chirplets [24]. The number of time-localized wavelets and their parameters are determined via the reversible jump Markov chain Monte Carlo algorithm. After that, whether the likelihood of the event is favored to be a true gravitational wave signal or instrumental glitch is determined by using a Bayesian model selection strategy. Finally, the posterior samples are used to reconstruct the signal as a superposition of the wavelets.

A wavelet can be regarded as a time-frequency localized bandpass filter. The bandwidth of which is determined by the properties of that wavelet. The reconstructed signal has an inevitable noise contribution that passes through those wavelet filters. The match between the reconstructed signal and the estimated waveform increases with the signal-to-noise ratio (SNR). However, we would never achieve absolute agreement (unit match) even if our predicted theory is complete because of the additional noise that passes through the coherent wavelets.

In this paper, we propose a quasi-model-dependent method for reconstruction of signal from noisy data. We identify the essential wavelets using binary black hole merger waveforms estimated using standard Bayesian analysis [25–28]. The unmodeled reconstruction methods identify the wavelets that are coherent across the network of detectors. The collection of those coherent wavelets in the time-frequency plane forms a cluster. Similarly, the essential wavelets form a cluster in the time-frequency plane which can be collectively viewed as a single patch with an irregular boundary.

The patch area determines how much noise persists in the reconstructed signal. The wavelets are discretely placed over the timescale plane, where the patch area is determined by the placement method and sparseness. The dyadic grid placement is considered to be the most efficient method, leading to the construction of an orthonormal wavelet basis. This placement assumes an output of octave decomposition (power-of-2 logarithmic) to construct the grid. The sparseness of the grid imposes a limit on the acceptable loss in signal characteristics. We target to achieve maximum sparseness and still have an adequate representation. A highly sparse grid might provide a sufficient signal representation, but the area covered by the essential wavelets would be larger than the case of a denser grid. In contrast, an overdense grid cannot reduce the patch area beyond a specific limit and also increases the computational cost.

In this paper, we propose a log-uniform scale to place the wavelets over the timescale domain. Further, we derive an inverse wavelet transformation formula for the log-uniform scale. The wavelets with such scales are highly redundant (i.e., overcomplete), but they can further reduce the area covered by the essential wavelets. As a result, We can reduce the noise contribution in the reconstructed signal, which leads to a more accurate signal reconstruction. Moreover, the essential wavelets with log-uniform scale can provide a more appropriate signal representation than the octave scale for the

high-frequency linear chirp signals. It implies that the log-uniform scale is more efficient for reconstructing the signals from low mass binary systems.

This paper is organized as follows: Section II describes the reconstruction methods using the continuous wavelet transformation with octave and log-uniform scales. Section III demonstrates the performance of the reconstruction methods for the linear chirp signals and gravitational wave signals in simulated Gaussian noise. Section IV describes the efficiency of the wavelet reconstruction method when a signal in the data does not belong to the manifold of the search template waveform by injecting an eccentric waveform. Section V exhibits results of our analysis for binary black hole merger events observed by the Advanced LIGO and Virgo detectors during the first and second observation runs. Finally, we conclude in Sec. VI.

II. RECONSTRUCTION FORMULAS FOR NONORTHOGONAL WAVELETS

The CWT of a continuous signal $x(t)$ is a linear mapping onto a timescale space of wavelets:

$$
\begin{aligned}
X(a, b) &= \int x(t)\, \Psi_{a,b}^{*}(t)\, dt \\
&= \frac{1}{\sqrt{a}} \int x(t)\, \psi^{*}\left(\frac{t-b}{a}\right) dt,
\end{aligned}
\tag{1}
$$

where ψ^{*} is the complex conjugate of the shifted and scaled version of the time-localized mother wavelet ψ, in which a and b are the scale and time-shift parameters, respectively. Therefore, the CWT provides a timescale representation of the signal by performing a sliding cross-correlation with a continuous family of wavelets. The quantity $1/\sqrt{a}$ outside the integral is an energy normalized factor. It assures that each wavelet has the same energy, whatever the value of scaling and shift. The function $\psi(t)$ must satisfy a set of mathematical criteria to be a wavelet, it must have finite energy,

$$
E_{\psi} = \int_{\infty}^{\infty} |\psi(t)|^{2}\, dt < \infty,
\tag{2}
$$

and must follow the admissibility condition

$$
C_{\psi} = \int_{\infty}^{\infty} \frac{|\tilde{\psi}(\omega)|^{2}}{\omega}\, d\omega < \infty,
\tag{3}
$$

where $\tilde{\psi}(\omega)$ is the Fourier transform of $\psi(t)$, $\omega = 2\pi f$ is the angular frequency, and C_{ψ} is called the admissibility constant. The above condition implies that $\tilde{\psi}(\omega)$ approaches zero faster than ω and must not have zero frequency component, $\tilde{\psi}(0) = 0$. If the wavelet function satisfies both criteria, then the inverse wavelet transform can be described as a superposition of the dual wavelets:

$$
x(t) = \frac{1}{C_{\psi}} \int_{0}^{\infty} \int_{-\infty}^{\infty} X(a, b)\, \Psi_{a,b}(t)\, \frac{1}{a^{2}}\, db\, da.
\tag{4}
$$

An alternative approach by inversion formula was found by Morlet; we can even choose a completely different wavelet function, a Dirac δ function $\delta((b-t)/a)$ instead of the analyzing wavelet, and that leads to a single integral inverse formula

[29],

$$x(t) = \frac{2}{C_\delta} \int_0^\infty \text{Re}\,\{X(a,t)\} \frac{1}{a^{3/2}}\, da, \qquad (5)$$

where C_δ is the admissibility constant of the δ function that can be computed using Eq.(3). In this work, we use this single integral inversion formula for reconstructing the gravitational wave signals.

The wavelet function can be regarded as an impulse response of a bandpass filter. The associated frequency of the wavelet can be treated as frequency value in the time-frequency domain, which is known as the pseudofrequency (f_p). It depends on the central frequency (f_c) and the scale parameter of the wavelet,

$$f_p = f_c/a \qquad (6)$$

This equation can used to represent the CWT in the time-frequency frame similarly to the short-time Fourier transform.

One of the most commonly used mother wavelets is the Morlet wavelet [30], which is a complex nonorthogonal wavelet. As a complex wavelet can separate the phase and amplitude components associated with the signal, it is more suited to determine the instantaneous frequency. The Morlet wavelet consists of a harmonic oscillation with Gaussian window,

$$\psi(t) = A_{f_c} \pi^{-1/4} (e^{i2\pi f_c t} - e^{-(2\pi f_c)^2/2}) e^{-t^2/2}, \qquad (7)$$

where $A_{f_c} = (1 - e^{-4\pi^2 f_c^2} - 2e^{-3\pi^2 f_c^2})^{-1/2}$ is the normalization constant. The second term in the parentheses is a correction to preserve the admissibility condition. It ensures that the zero-frequency component vanishes. In practice, we ignore this term as it is approximately zero for values of $f_c \gg 0$. Note that the above equation does not contain the time-shift and scale parameters. When we analyze a signal, we replace the variable t with $(t - b)/a$.

The central frequency f_c is a crucial parameter in the time-frequency analysis to regulate the tradeoff between temporal precession and spectral resolution. It controls the number of cycles of the wavelet without modifying the shape of the Gaussian window. A large value of central frequency leads to an increased temporal precision at the cost of decreased spectral precision and vice versa for a smaller value of central frequency. It is impossible to achieve simultaneously good precision in time as well as in frequency. A rule of thumb can be proposed for analyzing the gravitational waves from compact binary mergers. The signals from low-mass systems spend several tens of seconds or more than a hundred seconds in the bandwidth of Advanced LIGO–like detectors, looking like long-duration chirp signals. A larger value of central frequency is convenient to achieve an overall good time-frequency precision for those systems. On the other hand, a smaller value of central frequency is suitable for high mass systems as their signals are short-duration bursts with a tiny chirp.

A. Choice of wavelet scales: Octave

The CWT generally suffers due to the redundancy at large scales, where the neighboring wavelets are highly correlated. Once a wavelet function is chosen, it is important to choose the tightest set of scales that forms an orthonormal wavelet set. The key mathematical criterion to choose a set of discrete wavelets is that every function $f \in L^2(\mathbb{R})$[1] must be fully expressed as a superposition of those wavelets, i.e., the set is complete in $L^2(\mathbb{R})$. The conventional approach of choosing the scales is an output of octave decomposition [31,32],

$$a_j = a_0\, 2^{j\delta j}, \quad j = 0, 1, 2, \ldots, J,$$
$$J = \delta j^{-1} \log_2 (N\delta t/a_0), \qquad (8)$$

where N is the total number of samples in $x(t)$, δt is sampling interval, $a_0 = 2\delta t\, f_c$ is the smallest resolvable scale, and δj is the spacing between the discrete scales. For Morlet wavelets, an adequate scale resolution can be achieved for the values of $\delta j \lessapprox 0.5$. The quantity J that determines the highest value of the scale is associated with the Nyquist frequency. The octave scale leads to a simpler implementation of inverse discrete wavelet transformation as the quantity $da/a = a_0 \delta j \ln(2)$ is a constant. Now, the inverse formula Eq. (5) yields

$$x_n = \frac{\delta j \delta t^{1/2}}{C_\delta \psi_0(0)} \sum_{j=1}^J \frac{\text{Re}\,\{X_n(a_j)\}}{a_j^{1/2}}. \qquad (9)$$

B. Choice of log-uniform scale

For nonorthogonal wavelet analysis, one can adopt an arbitrary set of scales to build up a more complete picture if that set satisfies the completeness criteria. We propose a log-uniform scale,

$$\frac{1}{a_j} = \frac{1}{a_{j-1}} - \delta\ell = \frac{1}{a_0} - j\delta\ell. \qquad (10)$$

The quantity $\delta\ell = \delta f_p/f_c$ stands for the inverse of spacing between two discrete wavelets and the smallest resolvable scale $a_0 = f_c/\delta f_p$. In this work, we choose $\delta f_p = 1/T$, where T is duration of the time series. The log-uniform scale leads to an uniformly spaced pseudofrequency. In this formalism, Morlet wavelet transformation is equivalent to the scaled Gabor transformation as the pseudofrequencies are uniformly spaced. For log-uniform scale $da/a^2 = \delta\ell$, thus, the discrete inverse formula (5) yields

$$x_n = \frac{\delta\ell\, \delta t^{1/2}}{C_\delta\, \psi_0(0)} \sum_{j=1}^J a_j^{1/2}\, \text{Re}\,\{X_n(a_j)\}. \qquad (11)$$

C. Identifying the essential wavelets

The conventional method for identifying essential wavelets is a straightforward approach, where one discards the low-magnitude wavelet coefficients by applying a threshold, which is known as wavelet thresholding [33,34]. This approach aims to remove the noise from data without affecting the basic features of the signal. In this work, we propose a slightly different approach. We employ the modeled waveforms that are obtained from the standard Bayesian parameter estimation analysis. We compute wavelet coefficients for a waveform

---

[1]$L^2(\mathbb{R})$ denotes the space of square integrable functions on the real line ($\mathbb{R}$).

and set a threshold on coefficient value to select the essential wavelets. The threshold is chosen such that the resultant power from the essential wavelets is equal to a percentage of total power of the spectrogram. We calculate the threshold (E_*) for a given value of fractional power loss (R_*) by solving an equation,

$$R_* = 1 - \sum_{n,j} |X(n, j)|^2 \left[|X(n, j)|^2 \geqslant E_* \right] \Big/ \sum_{n,j} |X(n, j)|^2. \tag{12}$$

We shall call that R_* the spectral loss parameter. As the number of essential wavelets is considerably fewer than the total number of wavelets, a significant amount of noise can be removed while preserving the basic features of the signal.

D. Area occupied by the essential wavelets

Reconstructing a signal using the essential wavelets trades sensitivity, by which we are able to remove the noise from data. However, the reconstructed signal would always contain a nominal amount of inseparable noise, which passes through the wavelet filters. As a wavelet is regarded as a time-localized bandpass filter, it can be seen as a patch on the time-frequency plane. The area (time-frequency bandwidth) of that patch can be used to determine the amount noise released through that wavelet. Therefore, the total amount of inseparable noise can be estimated by calculating the total area covered by the essential wavelets.

The area on the time-frequency plane covered by a cluster of wavelets $\{(b_i, a_i)\}_{i=1}^{n_0}$ is related to their placement. For octave scale wavelets with a central frequency of f_c, the covered area is

$$A_{\text{Octave}} = \delta t \, a_0 \delta j \ln(2) \sum_{i=1}^{n_0} a_i$$
$$= 2 \ln(2) \, \delta j (f_c \delta t)^2 \sum_{i=1}^{n_0} 1/f_{pi}, \tag{13}$$

where f_{pi} is the ith pseudofrequency, $f_{pi} = f_c/a_i$. The time-frequency area governed by a cluster of wavelets $\{(b_i, a_i)\}_{i=1}^{n_0}$ with log-uniform scale is

$$A_{\text{log-uniform}} = \sum_{i=1}^{n_0} \delta t/T. \tag{14}$$

Figure 1 shows that the log-uniform scale occupies a smaller area than the octave scale. The figure indicates that the log-uniform scale allows $\sim 13\%$ less noise in the reconstructed signal than the octave scale for a high mass system, but can provide a nearly identical signal representation.

III. PERFORMANCE OF THE RECONSTRUCTION PROCEDURES

In this section, we demonstrate the performance of the wavelet based signal reconstruction and compare between the choice of octave and log-uniform scales. First, we exhibit that the essential wavelets are adequate to represent a chirp signal containing a broad range of frequencies. Second, we carry out injection analysis to evaluate the performance for real data
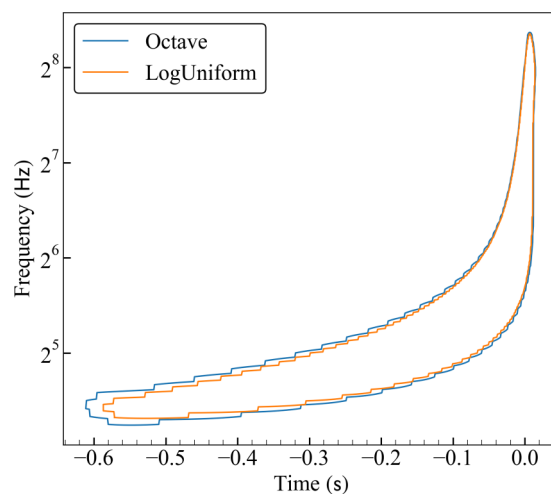

FIG. 1. An illustration of the area covered by the cluster of essential wavelets is produced using a gravitational waveform of a nonspinning equal mass binary system with a chirp mass of $30M_\odot$. The areas bounded by the log-uniform wavelets and octave scale wavelets are 13 and 15, respectively. For this computation, we have assumed an aLIGO [35] noise curve with a fixed lower cutoff frequency of 20 Hz, and the waveform is generated using the SEOBNRv4 model [36]. We have considered $R_* = 0.05$ for determining the essential wavelets.

analysis. The gravitational wave signals are drawn from a binary black hole merger and added to a simulated Gaussian noise.

A. Reconstruction of chirp signal without noise

We consider a simple chirp signal with a constant amplitude and phase up to a quadratic order in time (t),

$$x(t) = \sin(2\pi f_0 t + 2\pi f_0 t^2), \tag{15}$$

where f_0 is the starting frequency of the signal and the time range is chosen to be between 0 and 2 s. Therefore, the ending frequency of the chirp is $3f_0$. This type of chirp signal is adequate to exhibit the performance of the reconstruction method over a broad range of frequencies. We consider five different cases to identify the essential wavelets. For each case, the total power contained in the essential wavelets equals a fraction of signal power.

It is inevitable to have an overall amplitude loss since the number of essential wavelets is a small subset of the set of wavelets representing the whole timescale space. However, for a given value of R_*, we can set the overall amplitude by looking at the amplitude loss when determining the essential wavelets. An alternative approach is to define normalized minimum squared error (NMSE) for a reconstructed signal $x_{\text{rec}}(t)$,

$$\mathcal{E}_{\text{NMSE}} = \int |x(t)/\|x\| - x_{\text{rec}}(t)/\|x_{\text{rec}}\||^2 \, dt, \tag{16}$$

where the symbol $\|\cdot\|$ denotes the norm. We use the above equation to quantify the adequateness of the essential wavelets to characterize a linear chirp signal.

In Fig. 2, we illustrate the accuracy of the wavelet reconstruction of the linear chirp signals. The solid and dashed
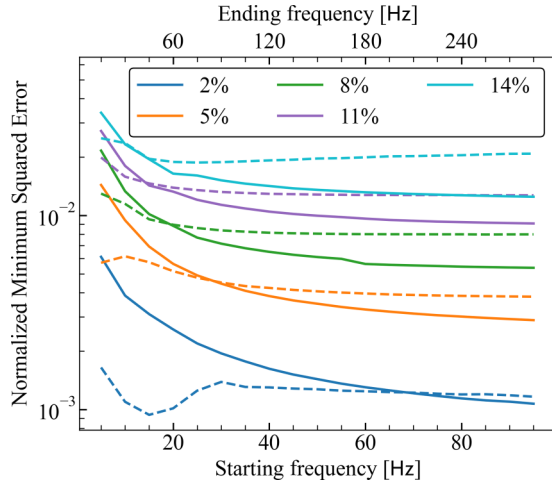
FIG. 2. Performance of octave and log-uniform scale wavelet reconstruction for linear chirp signals. The signals are generated using Eq. (15). The y-axis represents the normalized minimum squared error in the reconstructed signal. The solid line and dashed line correspond to the log-uniform scale and octave scale, respectively. The bottom and top x axes represent the starting and ending frequencies of the chirp, respectively. The legend represents a set of spectral loss parameters (R_*) as described in Eq. (12). We used those values to choose the essential wavelets.

lines correspond to the log-uniform scale and octave scale, respectively. We consider five different cases of fractional loss in spectrogram power to select the essential wavelets used for reconstruction. The reconstruction of high-frequency chirps using log-uniform scale wavelets is more accurate than the octave scale and vice versa for the low-frequency chirps.

B. Reconstruction of gravitational wave signal in simulated noise

We estimate the performance of the reconstruction methods for gravitational wave signals from compact binary mergers of equal mass nonspinning black holes. For each case, an identical signal is injected in many noise realizations of stationary Gaussian distribution weighted by Advanced LIGO zero-detuned high-power (aLIGO) design sensitivity [35]. The waveforms are generated for an wide range of chirp masses between $10M_\odot$ and $40M_\odot$ using the SEOBNRv4 model [36] with a fixed lower cutoff frequency of 20 Hz. To determine the reconstruction accuracy with signal-to-noise ratio (SNR) of the injection (injected SNR), we choose a set of values between 5 and 50. The injected SNR ($\rho_{\rm inj}$) of a waveform ($h_{\rm inj}$) is defined as

$$\rho_{\rm inj}^2 = 4 \int_{f_{\rm low}}^{f_{\rm high}} \frac{\tilde{h}_{\rm inj}^*(f)\,\tilde{h}_{\rm inj}(f)}{S_n(f)}\,df, \tag{17}$$

where $\tilde{h}_{\rm inj}(f)$ denotes the Fourier transform of $h_{\rm inj}(t)$ and $S_n(f)$ denotes the one-sided detector noise power spectral density.

We reconstruct the signal from noisy data using the log-uniform scale wavelet transform, where the essential wavelets are selected using Eq. (12). To quantify the signal reconstruction accuracy, we calculate the *match* between the injected

signal $h_{\rm inj}$ and reconstructed signal $h_{\rm rec}$, which is defined as the inner product between two normalized waveforms ($\hat{h}_* = h_*/\sqrt{\langle h_* \,|\, h_* \rangle}$):

$$\mathscr{M}(h_{\rm inj}, h_{\rm rec}) := \langle \hat{h}_{\rm inj} \,|\, \hat{h}_{\rm rec} \rangle, \tag{18}$$

where the term within angular brackets represents the following inner product:

$$\langle h_{\rm inj} \,|\, h_{\rm rec} \rangle = 4\,{\rm Re} \int_{f_{\rm low}}^{f_{\rm high}} df\,\frac{\tilde{h}_{\rm inj}^*(f)\,\tilde{h}_{\rm rec}(f)}{S_n(f)}, \tag{19}$$

where $\tilde{h}_{\rm inj}(f)$ and $\tilde{h}_{\rm rec}(f)$ denote the Fourier transforms of $h_{\rm inj}(t)$ and $h_{\rm rec}(t)$, respectively.

The match between two waveforms varies between -1 and 1, depending on their correlation but not their overall amplitudes. A match value of 1 indicates a perfect positive correlation such that two waveforms change with equal proportion, and 0 means no correlation. The equal proportion changes with reverse direction indicate perfect negative correlation, for which match value is -1. To quantify the agreement between the wavelet reconstruction for a network of detectors, we compute the network match ($\mathscr{M}_{\rm net}$) as given in [37],

$$\mathscr{M}_{\rm net} = \frac{\sum_k \langle h_{\rm inj}^k \,|\, h_{\rm rec}^k \rangle}{\left(\sum_k \langle h_{\rm inj}^k \,|\, h_{\rm inj}^k \rangle \cdot \sum_k \langle h_{\rm rec}^k \,|\, h_{\rm rec}^k \rangle \right)^{1/2}}, \tag{20}$$

where k represents the kth detector. In this paper, we consider the three-detector configurations of Hanford (H1), Livingston (L1), and Virgo (V1). We consider aLIGO design sensitivity for H1 and L1 detectors [35,38,39], and advanced Virgo design sensitivity for V1 [40,41]. Please note that we demonstrate the injection analysis in this section assuming a single detector with the aLIGO design sensitivity.

A whitened Gaussian noise is considered to be distributed normally over the timescale domain. This implies that the noise energy is equally distributed over the timescale domain. The amount of noise retained in the reconstructed signal is determined by the spectral loss parameter R_*. A higher value of R_* can further reduce the inseparable noise in the reconstructed signal. At the same time, the essential wavelets would not be able to represent the complete signal characteristics. It implies that the spectral loss parameter plays a role that imposes a limitation on achieving the maximum overlap between the injected and reconstructed signals. Therefore, we want to optimize this parameter. For a given source parameter and injected SNR, we perform the injection analysis with a set of R_* values. The noise averaged match for a given injected signal $h_{\rm inj}(\vec{\lambda}, \rho_{\rm inj})$ and R_* can be defined as

$$\langle \mathscr{M}(R_*) \rangle_{\rm noise} = \frac{1}{N} \sum_{i=1}^{N} \mathscr{M}(h_{\rm inj}, h_{\rm rec}[n_i]), \tag{21}$$

where $h_{\rm rec}[n_i]$ represents the reconstructed signal from the data of ith noise realization n_i. To determine the essential wavelets for a given value of R_*, we compute the wavelet coefficients of the whitened waveform and plug them into Eq. (12).

Figure 3 shows the noise averaged match as a function of R_* for a set of injected SNR values and the number of essential wavelets as a function of R_*. If we fix the spec-
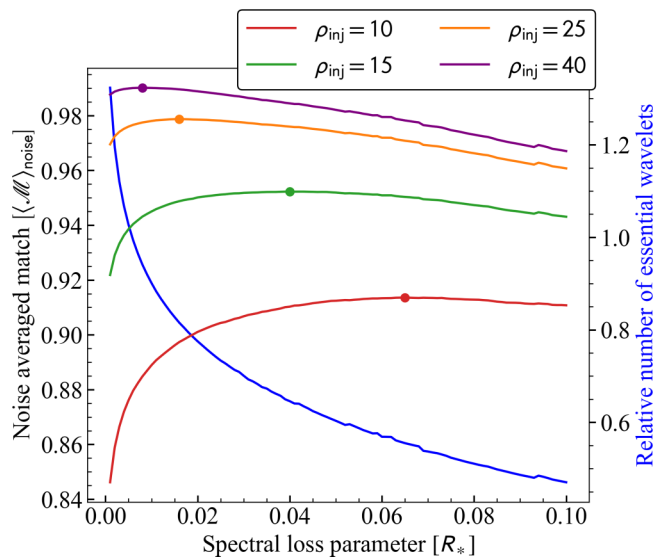
FIG. 3. The noise averaged match ($\langle \mathcal{M} \rangle_{\text{noise}}$) as a function of spectral loss parameter (R_*) is produced using a gravitational waveform of a nonspinning equal mass binary system with a chirp mass of $30 M_\odot$. The solid dot on the curve indicates its maximum. The right y axis shows the relative number of essential wavelets ($\bar{N}_W$) as a function of R_*. The unit value of $\bar{N}_W$ corresponds to a 99.9% match between the original and reconstructed signals for the zero noise case. These results are produced assuming the aLIGO noise curve with a fixed lower cutoff frequency of 20 Hz. The waveforms are generated using the SEOBNRv4 model.
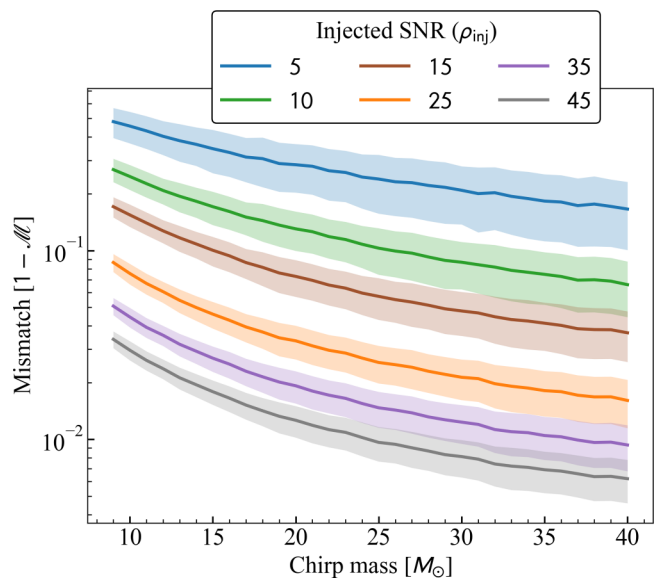

FIG. 4. The figures shows the mismatch between the injected gravitational wave signal and reconstructed signal, where the filter wavelets were constructed using the log-uniform scale as defined in Eq. (10). To produce the injections, we have assumed nonspinning equal mass binary black holes with a wide range of chirp mass as labeled in the x axis. The legend indicates the optimal SNR of the injected signal. We have injected an identical signal into many noise realization to produce the distribution of mismatch for each chirp mass. We have assumed the aLIGO noise curve with a fixed lower cutoff frequency of 20 Hz. The waveforms are generated using the SEOBNRv4 model.

tral loss parameter and increase the injected SNR, the signal contribution to each essential wavelet increases. At the same time, the average noise contribution remains the same since the number of essential wavelets and their properties does not change. This leads to an improvement in the reconstruction accuracy. A fixed SNR curve in Fig. 3 indicates that a smaller value of R_* allows many nonessential wavelets in the analysis. The signal contribution to those wavelets is trivial, but the inseparable noise in the reconstructed signal increases. On the other hand, a higher value of R_* discards many moderate essential wavelets. Thus, the choice of R_* is a tradeoff between the signal and noise contributions to the wavelets. To find an optimum value R, we maximize the quantity $\langle \mathcal{M}(R_*) \rangle_{\text{noise}}$ over R_*.

Figure 4 demonstrates the *mismatch* $(1 - \mathcal{M})$ in reconstruction for nonspinning binary systems with equal component masses. The solid curve represents the median of the mismatch distribution, and the shaded region shows the $\pm\sigma$ width of that distribution. For the case of a fixed optimal SNR, we can see that mismatch substantially decreases with an increase of chirp mass. It is intuitively expected: the number of essential wavelets for high chirp mass systems is fewer than in low chirp mass systems. The waveform of a binary system with high chirp mass can be characterized using a few wavelets as the waveform is short. In contrast, the waveform of a low chirp mass system is longer, for which one requires a large number of wavelets to represent the signal.

As the injection chirp mass increases, the number of essential wavelets decreases, and they cover a smaller area over the time-frequency plane. The signal contribution to the essential

wavelet coefficients increases with the injection chirp mass for a fixed SNR case. At the same time, the noise contribution decreases due to the smaller area. That explains why the reconstruction signal for a high chirp mass system is more accurate than that of a low chirp mass.

IV. IDENTIFYING THE DEVIATION

So far, we have discussed the performance of wavelet reconstruction where injected waveforms were used for determining the essential wavelets. Those results tell us the efficiency of the semi-model-dependent wavelet reconstruction method when a signal in the data belongs to the search template waveform manifold. However, a signal in real data may not belong to that manifold. Deviations could arise due to the influence of unknown binary parameters (such as eccentricity if the waveform model only considers the circular binary), missing physics in the waveform model, deviation from GR, or noise artifacts. We demonstrate one of such cases, an injection waveform simulation for an eccentric BBH merger. Since recent template-based analysis by LIGO and Virgo Collaborations (LVC) used a quasicircular waveform [4], we consider the recently developed IMRPhenomXP model to generate the template waveform [42]. This model includes the effect of orbital precession but does not consider orbital eccentricity.

The inclusion of eccentricity in the injected signal leads to a deviation from the search template waveform
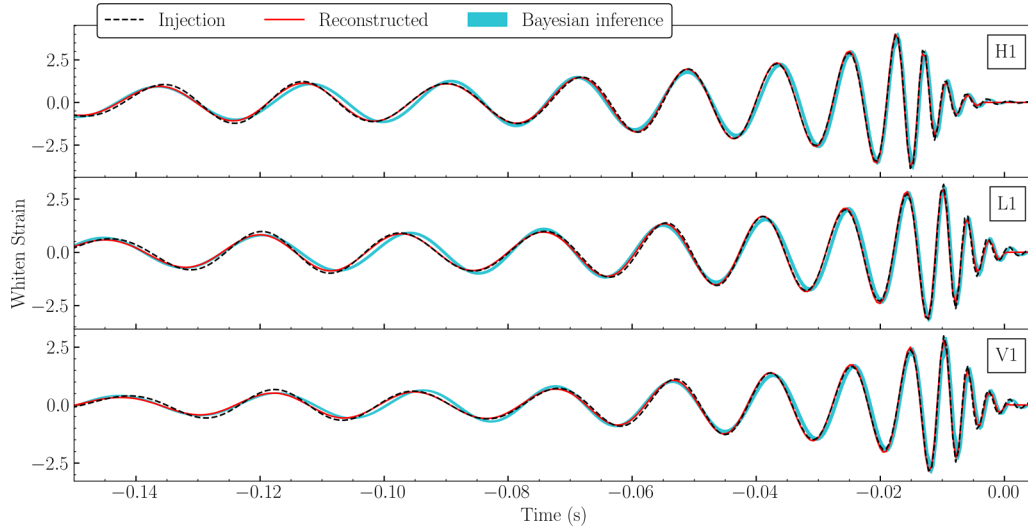
FIG. 5. An illustration of wavelet reconstruction (solid red line) and LALINFERENCE (cyan band) with the IMRPhenomXP waveform model, obtained from an injection analysis using an eccentric numerical relativity waveform SXS:BBH:0323 picked from thr SXS catalog with a total mass of $60M_\odot$. The dashed black line represents the injected waveform. For this computation, we have used the three-detector configuration of Advanced LIGO and Advanced Virgo.

manifold. To demonstrate this, we consider a numerical-relativity simulation of an eccentric inspiral-merger-ringdown (IMR) waveform picked from the Simulating eXtreme Space-times (SXS) catalog [43]. This system is a nonspinning binary with mass ratio of 1.22. The numerical simulation is performed for an eccentric BBH system, where eccentricity evolves with time. The reference eccentricity is $e_{ref} = 0.194$ as measured at a reference orbital frequency of $Mf_0 = 0.0137$. In our analysis, we scale the simulation for a total mass of $60M_\odot$, which is suitable for ground based detectors.

We keep the system in the *face-on* configuration where the inclination angle is 0°. As the component masses are nearly equal and zero inclination, the contribution of higher-order modes to the injected signal is negligible. This configuration assures us that the deviation enters only due to the orbital eccentricity. We inject the signal assuming the three-detector configuration of Advanced LIGO and Advanced Virgo [35,38–41]. We set the source's sky position and distance such that the injected SNR in H1, L1, and V1 are 25, 20, and 15, respectively. Since the average result of our wavelet reconstruction over many Gaussian noise realizations with an identical injected signal leads to the case of zero noise, we consider a zero-noise realization to construct the data stream. We analyze the data using the standard Bayesian parameter estimation library LALINFERENCENEST [27], a Bayesian inference nested sampling code implemented in the LIGO Algorithm Library (LALSUITE) [44]. We use the python-based package PESUMMARY [45] to process the data from parameter estimation analysis and generate the template waveform in the detector frame.

In order to reconstruct the signal from data stream, we follow these steps:

(1) For each posterior sample, we generate the CBC template waveform in the detector frame. Since GR allows only two polarization states, referred to as the plus (h_+) and cross ($h_\times$), the time-domain response $h_\mathcal{I}(t)$ of a given detector $\mathcal{I}$ is determined by the antenna response functions ($F_\mathcal{I}^+$ and $F_I^\times$) of those polarizations [46],

$$h_\mathcal{I}(t) = F_\mathcal{I}^+(\alpha, \delta, \psi, t)h_\times(t - \Delta t_\mathcal{I}; D_L, \iota, \vec{\lambda})$$
$$+ F_\mathcal{I}^\times(\alpha, \delta, \psi, t)h_+(t - \Delta t_\mathcal{I}; D_L, \iota, \vec{\lambda}), \quad (22)$$

where α and δ denote the source sky location in terms of right ascension and declination, ψ is the polarization angle, D_L is the luminosity distance to the source, ι is the inclination angle of the binary plane, $\vec{\lambda}$ represents the set of intrinsic parameters of the binary system, and $\Delta t_\mathcal{I}$ [$\equiv \Delta t_\mathcal{I}(\alpha, \delta, t)$] is the travel time of the signal from geocenter to the detector.

(2) Whiten the waveform weighted by the noise amplitude spectral density such that the norm of the whitened waveform is equal to its optimal SNR.

(3) Compute the wavelet coefficients for each whitened template waveform using the CWT as shown in Eq. (1), where wavelets are constructed using the log-uniform scale.

(4) Determine the essential wavelets using Eq. (12), where spectral loss parameter R_* is obtained from Eq. (21). We inject the best fit template (corresponding to the maximum likelihood sample) waveform in many simulated noise realizations and estimate the value of R_* for each detector's data. We have found that the values of R_* for H1, L1, and V1 are 2.5%, 4%, and 5%, respectively. Please note that we estimate the spectral loss parameter for the maximum likelihood sample and use that value for all the posterior samples.

(5) Use those essential wavelets to reconstruct the signal from detector strain.

The above-described procedure is used to obtain a reconstructed signal for each posterior sample. These wavelet-based reconstructed signals are very similar, and their 90% interval is very thin and looks like a line. Therefore, we illustrate the median of reconstructed signals at every time index.[2]

---

[2]Note that the median of the reconstructed signals is used *only* for the illustration in time-domain.

TABLE I. Comparison between the LALINFERENCE template waveform and log-uniform wavelet reconstruction for an eccentric numerical relativity waveform SXS:BBH:0323 picked from SXS catalog with a total mass of $60M_\odot$. The numerical simulation is performed for a nonspinning, nearly equal-mass eccentric BBH system, where the measured reference eccentricity is $e_{ref} = 0.194$ at a reference orbital frequency of $Mf_0 = 0.0137$. The quantity $\widetilde{\mathscr{M}}$ denotes the median of the match values.

Detector	ρ_{inj}	$\widetilde{\mathscr{M}}_{bif}^{inj}$	$\widetilde{\mathscr{M}}_{bif}^{rec}$	$\widetilde{\mathscr{M}}_{rec}^{inj}$	$\widetilde{\rho}_{res}$
Hanford (H1)	25	0.954	0.968	0.984	6.2
Livingston (L1)	20	0.95	0.959	0.978	5.5
Virgo (V1)	15	0.959	0.959	0.978	4.2
Network	35.6	0.949	0.958	0.981	

Figure 5 illustrates the results from wavelet reconstruction, 90% credible region of LALINFERENCE template waveform, and injected waveform. We can see the amplitude and phase of the reconstructed waveform are approximately consistent with the injected waveform. In contrast, the LALINFERENCE waveform is out of phase over a bit of the region, which indicates a significant deviation from the search template waveform manifold. We also compute three different matches using the reconstructed signal (h_{rec}), LALINFERENCE template waveform (h_{bif}) obtained from posterior samples as described in step 1, and injected waveform (h_{inj}): $\mathscr{M}(h_{inj}, h_{bif})$, $\mathscr{M}(h_{bif}, h_{rec})$, and $\mathscr{M}(h_{inj}, h_{rec})$. Table I summarizes the match comparison. It signifies that the wavelet-based reconstructed waveform is more faithful than LALINFERENCE.

However, we cannot compute $\mathscr{M}(h_{rec}, h_{inj})$ and $\mathscr{M}(h_{bif}, h_{inj})$ for an actual event case as it is infeasible to know the true signal in data. We propose to compute the residual SNR (ρ_{res}) obtained by subtracting each template waveform of LALINFERENCE posterior samples from the corresponding wavelet-based reconstructed waveform. LVC commonly uses this procedure in the test of GR with BBH events [9–11,47]. We report the median of residual SNR in the last column of Table I.

V. ANALYSIS OF EVENTS IN GWTC-1

We apply the proposed method to each binary black hole event in the first gravitational-wave transient catalog GWTC-1 [3] to reconstruct the signals from individual detectors. In this analysis, we use the on-source data from the Gravitational Wave Open Science Center [48,49], released for GWTC-1 [3]. For determining the essential wavelets, we use the posterior samples of source properties obtained from reanalysis of GWTC-1 using BILBY [50,51]. Parameter estimation analysis was performed using the IMRPhenomPv2 [52,53] waveform model, and power spectral density was estimated using the BAYESLINE algorithm [54].

In order to reconstruct the signal from data using the posterior samples, we follow the steps described in Sec. IV. Figure 6 shows the results for GW150914 [1]: CBC template waveform from posterior sample and wavelet reconstruction. The agreement for H1 data is better than L1 data as the reconstruction accuracy increases with SNR. For H1 data, the most probable value (mode) of the match values is 0.975, and the maximum is 0.982. We also compute the network match values and their mode 0.962. It implies an excellent agreement between the GR template waveform and the observed data. We have seen that the reconstructed signal does remain
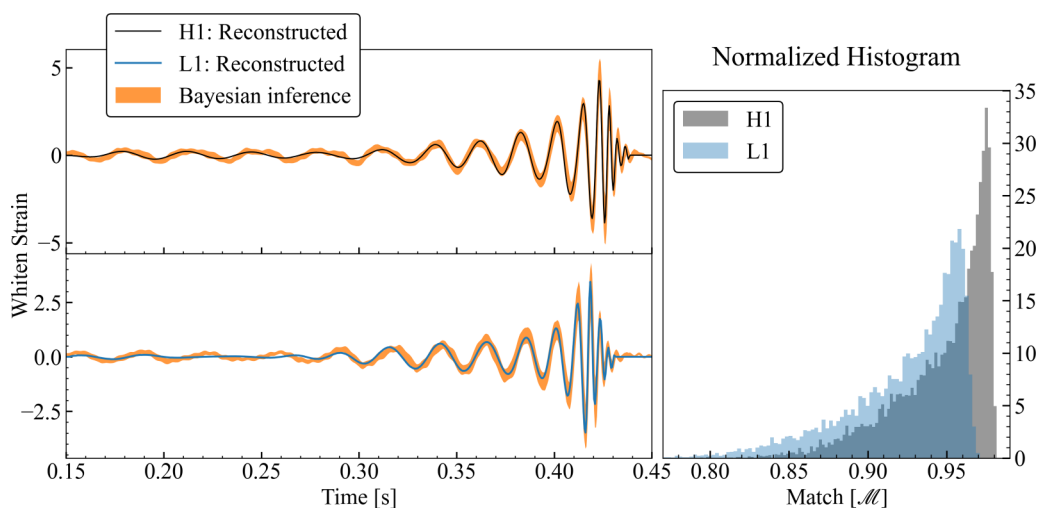

FIG. 6. Log-uniform scale wavelet reconstruction results of the GW150914 event, obtained using the on-source data of H1 and L1 detectors, where the times (in seconds) are shown relative to a reference time 1126259462.0. The solid black line in the top-left panel shows the median reconstructed signal obtained from H1 data and the solid blue line in the bottom-left panel from L1 data. The orange band in these panels is produced using the CBC template waveforms from parameter estimation samples. We demonstrate the reconstructed signals and CBC template waveforms in units of the standard deviation of the noise, which implies the norm is SNR. The right panel shows the histogram of the match between every posterior waveform and the corresponding wavelet-based reconstructed signal.

TABLE II. List of match values of GWTC-1 events obtained by computing the match between the reconstructed waveform and the Bayesian inference template waveform. We report the chirp mass and the SNR to indicate the efficiency of the reconstruction as demonstrated in Sec. III B. We report the median (denoted by tilde) value of the distribution. Dashes (–) correspond to a detector not being included in the analysis.

Event	$\widetilde{\mathcal{M}}_c$	$\widetilde{\rho}_{\rm bif}^{\rm H1}$	$\widetilde{\rho}_{\rm bif}^{\rm L1}$	$\widetilde{\rho}_{\rm bif}^{\rm V1}$	$\widetilde{\mathscr{M}}_{\rm H1}$	$\widetilde{\mathscr{M}}_{\rm L1}$	$\widetilde{\mathscr{M}}_{\rm V1}$	$\widetilde{\mathscr{M}}_{\rm net}$
GW150914	31.0	20.6	14.3	–	0.96	0.94	–	0.95
GW151012	18.3	6.5	5.9	–	0.73	0.74	–	0.73
GW151226	9.7	9.8	6.9	–	0.80	0.66	–	0.74
GW170104	25.7	9.5	10.0	–	0.86	0.89	–	0.87
GW170608	8.5	12.1	9.2	–	0.78	0.49	–	0.60
GW170729	51.5	6.0	8.3	1.7	0.89	0.91	−0.21	0.85
GW170809	29.7	6.0	10.8	1.1	0.86	0.92	0.02	0.89
GW170814	27.0	9.3	14.2	3.8	0.88	0.93	0.74	0.91
GW170818	32.1	4.7	9.8	4.3	0.80	0.90	0.82	0.87
GW170823	38.9	7.1	9.5	–	0.88	0.93	–	0.91

almost identical even when the essential wavelets are selected using different posterior samples. Therefore, we consider the case of the maximum likelihood sample only to illustrate the signal is time domain. Note that match values are computed between every posterior waveform and the corresponding wavelet-based reconstructed signal; we call this *on-source* match.

Our reconstruction method trades with sensitivity for identifying the essential wavelets and removing the noise from on-source data. Consequently, the technique cannot discern the early inspiral or late ringdown part of the CBC waveforms where the signals are weaker. In the time-frequency domain, the early inspiral part spreads over time, whereas the late-ringdown part of the signal spreads over the frequency direction. In Fig. 6, it is visible that the early inspiral part of the L1 signal (before 0.25 seconds) fades out. However, the H1 signal is still present and consistent with the template waveform because of the higher SNR in H1. At the same time, the late ringdown part of both the signals hasc disappeared. In a time-frequency frame, the ringdown part of a signal spreads out over frequency despite having a fixed frequency because of its exponential decay term, leading to a Lorentzian spread along the frequency direction.

Further, we perform the reconstruction analysis on the remaining events of GWTC-1 [55–59] and report the results in Table II. In order to understand the reconstruction efficiency depending on the SNR and chirp mass, we also reported them in the same Table. These values are obtained from the posterior samples by BILBY [51]. The solid vertical line in Fig. 7 shows the 90% interval of the on-source network match values, and the solid circle marks their mode value. We found the best agreement with GR for the GW150914 event, and the minimum for GW170608, albeit the observed SNR from the latter event was higher than the nominal threshold in both the detectors. The match value depends not only on SNR but also on the time-frequency area covered by the essential wavelets of the signal. In Sec. III B, we saw that the match value increases with injection chirp mass while the injection SNR is kept at a fixed value. GW170608 event has the lowest chirp mass in the catalog, for which its essential wavelets occupy the largest area over the time-frequency plane.

The vertical dashed line in Fig. 7 shows the 90% interval of expected match that is determined by injecting the maximum likelihood BILBY waveform ($h_{\rm bif}^*$) in many Gaussian noise realizations; a similar study is shown in Fig. 4. We have reconstructed the signal from each realization and computed the match with $h_{\rm bif}^*$. We see that there is significant overlap between the distribution of expected match and on-source match, except for GW151226 and GW170608. In particular, the distributions are far from each other for GW170608, for which a further study is worthy. We will focus on it in future work.

For GW170729, the match V1 datum is negative, which is unexpected. The reconstructed signal and template waveform
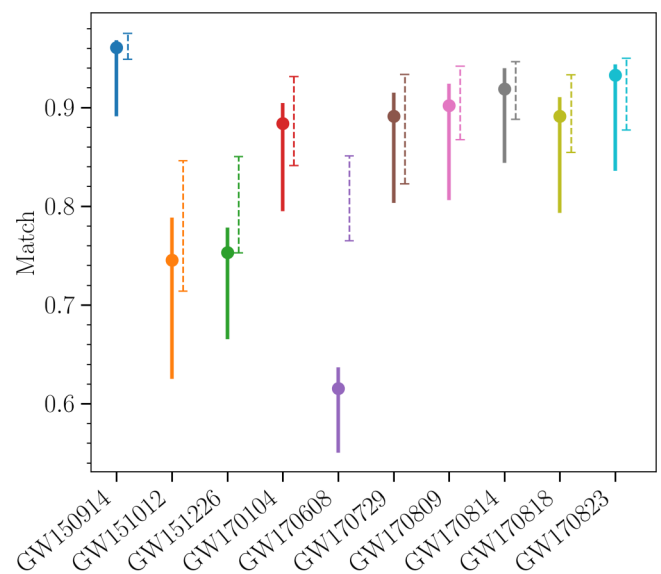

FIG. 7. Network match between the CBC template waveform by Bayesian parameter estimation and the wavelet-based reconstructed waveform. The vertical solid line represents the 90% credible interval of the on-source match. The dot over each line is the mode of the on-source match distribution. The vertical dashed line indicates the 90% interval of the expected match under the assumption of Gaussian noise, which is similar to Fig. 4.
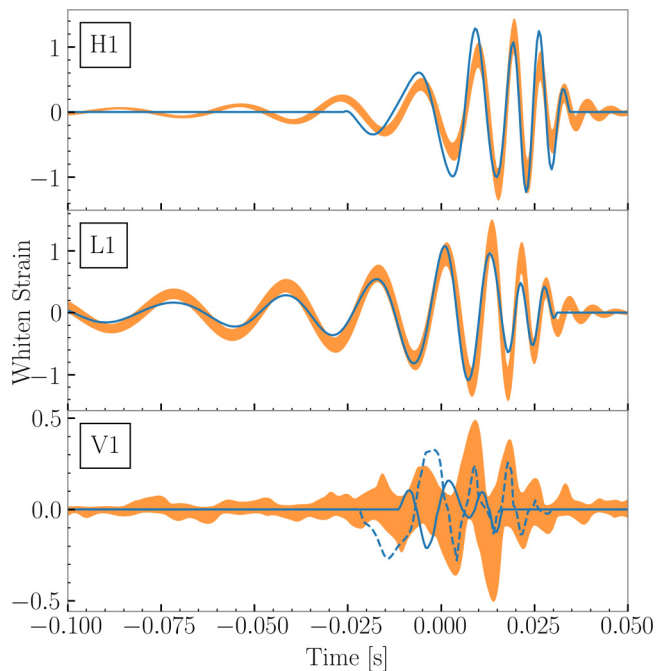
FIG. 8. Signal reconstruction results of GW170729 with a reference time 1185389807.3. We plot the 90% credible interval of the CBC template waveform (orange band) and median reconstructed signal (blue). The blue dashed line in the bottom panel shows the projected signal of H1 and L1 over V1, where the sky location and polarization angle are taken from parameter estimation samples.

are nearly in antiphase for most of the posterior samples, as shown in Fig. 8, leading to a negative match value. It could be due to the noise artifacts. The antiphase could occur due to poor constraint of event time in the detector frame. The total widths of event time distribution for H1, L1, and V1 are 19, 18, and 63 ms, respectively. The spread for V1 data is significantly larger than the other two. It is impossible to draw an appropriate conclusion about whether the deviation presents or not when the SNR is very low. Thereby, we also compute the network match excluding the contribution of V1. The median network match for two detectors is 0.88, and the mode is 0.89. An extensive study on agreement between the CBC template waveform and the BAYESWAVE reconstruction also found the similar results [60], where the contribution of V1 data was not considered for this study. We excluded the contribution of V1 for GW170729 to produce Fig. 7. As a further investigation, we project the H1 and L1 signals over V1 based on the sky location and polarization angle of parameter estimation samples. We follow these steps to obtain the projected signal: (a) perform the inverse transformation of the whitening procedure over H1 and L1 reconstructed signals and apply a time shift based on the sky location to obtain these signals in geocentric coordinates, (b) obtain the two GW polarizations based on the sky location and polarization angle, and (c) project on the frame of V1 detector as shown in the bottom panel (blue dashed curve) of Fig. 8. We can see that the projected signal and CBC template waveform are in phase, and the median match is 0.64. It implies that the noise probably plays a role in the V1 reconstructed signal being antiphase.

VI. CONCLUSION

This paper presents a wavelet-based semi-model-dependent method for reconstructing the gravitational wave signals produced from compact binary mergers. We have employed the framework of continuous wavelet transformation, where Morlet wavelets represent the signals. The semi-model-dependent approach determines the essential wavelets using the posterior samples from parameter estimation to reconstruct the signals from the data.

In general, the wavelets are constructed using an output of octave scale, which provides the tightest set of wavelets. Such wavelets yield a nearly orthogonal wavelet basis. In this paper, we have proposed a log-uniform scale for constructing the wavelets. Such wavelets are highly redundant, i.e., nonorthogonal wavelets. However, this new scale is more efficient for representing the linear chirp signals at high frequencies than the octave scale. As the wavelets are regarded as time localized bandpass filters, a reconstructed signal always contains a nominal amount of noise that passes through the essential wavelets. The amount of noise depends on the area covered by the essential wavelets over the time-frequency plane. We have shown that the essential wavelets with the log-uniform scale occupy a smaller space than with the octave scale, which enables us to reconstruct the weak signals better.

We have conducted injection analysis to evaluate the reconstruction efficiency for the signals from binary black hole mergers by computing the match between the injected waveform and the reconstructed signal. The reconstruction accuracy increases with the SNR such that the mismatch is approximately proportional to SNR squared, $1 - \mathscr{M} \gtrsim 1/\text{SNR}^2$. Also, the reconstruction accuracy strongly depends on chirp mass. We have seen that the mismatch at a fixed SNR decreases as chirp mass increases.

We have demonstrated the ability to detect the deviation where the injected waveform is outside the region of space enclosed by the search template waveform manifold. We have performed the parameter estimation analysis using LALINFERENCE by injecting an electric BBH waveform, where the template waveforms are generated by a quasicircular waveform model, IMRPhenomXP. After that, we studied the match between the injected waveform and the reconstructed waveform. As reported in Table I, the LALINFERENCE waveform agrees less with the injected waveform than the wavelet reconstruction. Also, the LALINFERENCE waveform is out of phase over a bit of the region. In comparison, the amplitude and phase of the reconstructed waveform are nearly consistent with the injected waveform.

We have applied this wavelet-based reconstruction analysis to each binary black hole merger event in GWTC-1. We have seen a satisfactory agreement between the reconstructed signal and the estimated theoretical waveform. As the gravitational wave catalog grows, we expect the wavelet-based semi-model-dependent reconstruction method to provide a more precise view of the agreement between the observed data and the waveform model.

There are many avenues for future work and extensions of this method: combining the octave and log-uniform scales to have an optimal method for reconstructing the signals from compact binaries; applying this new method for reconstruct-

ing the signal from binary neutron star mergers; developing appropriate statistics for detecting the deviations and investigating the match study when instrumental an glitch presents in on-source data; and applying this method to GWTC-2 and GWTC-3 [4,5].

ACKNOWLEDGMENTS

[1] B. P. Abbott *et al.* (LIGO Scientific Collaboration and Virgo Collaboration), Observation of Gravitational Waves from a Binary Black Hole Merger, Phys. Rev. Lett. **116**, 061102 (2016).

[2] B. P. Abbott *et al.* (LIGO Scientific Collaboration and Virgo Collaboration), GW170817: Observation of Gravitational Waves from a Binary Neutron Star Inspiral, Phys. Rev. Lett. **119**, 161101 (2017).

[3] B. P. Abbott *et al.* (LIGO Scientific Collaboration and Virgo Collaboration), GWTC-1: A Gravitational-Wave Transient Catalog of Compact Binary Mergers Observed by LIGO and Virgo during the First and Second Observing Runs, Phys. Rev. X **9**, 031040 (2019).

[4] R. Abbott *et al.* (LIGO Scientific Collaboration and Virgo Collaboration), GWTC-2: Compact Binary Coalescences Observed by LIGO and Virgo During the First Half of the Third Observing Run, Phys. Rev. X **11**, 021053 (2021).

[5] R. Abbott *et al.* (The LIGO Scientific Collaboration, the Virgo Collaboration, and the KAGRA Collaboration), GWTC-3: Compact binary coalescences observed by LIGO and Virgo during the second part of the third observing run, arXiv:2111.03606.

[6] T. Venumadhav, B. Zackay, J. Roulet, L. Dai, and M. Zaldarriaga, New search pipeline for compact binary mergers: Results for binary black holes in the first observing run of Advanced LIGO, Phys. Rev. D **100**, 023011 (2019).

[7] A. H. Nitz, C. Capano, A. B. Nielsen, S. Reyes, R. White, D. A. Brown, and B. Krishnan, 1-OGC: The first open gravitational-wave catalog of binary mergers from analysis of public Advanced LIGO data, Astrophys. J. **872**, 195 (2019).

[8] A. H. Nitz, T. Dent, G. S. Davies, S. Kumar, C. D. Capano, I. Harry, S. Mozzon, L. Nuttall, A. Lundgren, and M. Tápai, 2-OGC: Open Gravitational-wave Catalog of binary mergers from analysis of public Advanced LIGO and Virgo data, Astrophys. J. **891**, 123 (2020).

[9] B. P. Abbott *et al.* (LIGO Scientific Collaboration and Virgo Collaboration), Tests of General Relativity with GW150914, Phys. Rev. Lett. **116**, 221101 (2016); **121**, 129902 (2018).

[10] B. P. Abbott *et al.* (LIGO Scientific Collaboration and Virgo Collaboration), Tests of general relativity with the binary black hole signals from the LIGO-Virgo catalog GWTC-1, Phys. Rev. D **100**, 104036 (2019).

[11] R. Abbott *et al.* (LIGO Scientific Collaboration and Virgo Collaboration), Tests of general relativity with binary black holes from the second LIGO-Virgo gravitational-wave transient catalog, Phys. Rev. D **103**, 122002 (2021).

[12] S. Klimenko and G. Mitselmakher, A wavelet method for detection of gravitational wave bursts, Class. Quantum Grav. **21**, S1819 (2004).

[13] S. Klimenko, S. Mohanty, M. Rakhmanov, and G. Mitselmakher, Constraint likelihood analysis for a network of gravitational wave detectors, Phys. Rev. D **72**, 122002 (2005).

[14] S. Klimenko, I. Yakushin, A. Mercer, and G. Mitselmakher, A coherent method for detection of gravitational wave bursts, Class. Quantum Grav. **25**, 114029 (2008).

[15] N. J. Cornish and T. B. Littenberg, Bayeswave: Bayesian inference for gravitational wave bursts and instrument glitches, Class. Quantum Grav. **32**, 135012 (2015).

[16] N. J. Cornish, T. B. Littenberg, B. Bécsy, K. Chatziioannou, J. A. Clark, S. Ghonge, and M. Millhouse, BayesWave analysis pipeline in the era of gravitational wave observations, Phys. Rev. D **103**, 044006 (2021).

[17] P. J. Sutton *et al.*, X-Pipeline: An Analysis package for autonomous gravitational-wave burst searches, New J. Phys. **12**, 053034 (2010).

[18] S. Chatterji, A. Lazzarini, L. Stein, P. J. Sutton, A. Searle, and M. Tinto, Coherent network analysis technique for discriminating gravitational-wave bursts from instrumental noise, Phys. Rev. D **74**, 082005 (2006).

[19] S. Ghonge, K. Chatziioannou, J. A. Clark, T. Littenberg, M. Millhouse, L. Cadonati, and N. Cornish, Reconstructing gravitational wave signals from binary black hole mergers with minimal assumptions, Phys. Rev. D **102**, 064056 (2020).

[20] F. Salemi, E. Milotti, G. A. Prodi, G. Vedovato, C. Lazzaro, S. Tiwari, S. Vinciguerra, M. Drago, and S. Klimenko, Wider look at the gravitational-wave transients from GWTC-1 using an unmodeled reconstruction method, Phys. Rev. D **100**, 042003 (2019).

[21] W. G. Anderson, P. R. Brady, J. D. E. Creighton, and E. E. Flanagan, Excess power statistic for detection of burst sources of gravitational radiation, Phys. Rev. D **63**, 042003 (2001).

[22] V. Necula, S. Klimenko, and G. Mitselmakher, Transient analysis with fast Wilson-Daubechies time-frequency transform, J. Phys.: Conf. Ser. **363**, 012032 (2012).

[23] S. Klimenko *et al.*, Method for detection and reconstruction of gravitational wave transients with networks of advanced detectors, Phys. Rev. D **93**, 042004 (2016).

[24] M. Millhouse, N. J. Cornish, and T. Littenberg, Bayesian reconstruction of gravitational wave bursts using chirplets, Phys. Rev. D **97**, 104057 (2018).

[25] C. Röver, R. Meyer, and N. Christensen, Bayesian inference on compact binary inspiral gravitational radiation signals in interferometric data, Class. Quantum Grav. **23**, 4895 (2006).

[26] M. van der Sluys, V. Raymond, I. Mandel, C. Rover, N. Christensen, V. Kalogera, R. Meyer, and A. Vecchio, Parameter estimation of spinning binary inspirals using Markov-chain Monte Carlo, Class. Quantum Grav. **25**, 184011 (2008).

[27] J. Veitch *et al.*, Parameter estimation for compact binaries with ground-based gravitational-wave observations using the LAL-Inference software library, Phys. Rev. D **91**, 042003 (2015).

[28] J. Skilling, Nested sampling for general Bayesian computation, Bayesian Anal. **1**, 833 (2006).

[29] M. Farge, Wavelet transforms and their applications to turbulence, Annu. Rev. Fluid Mech. **24**, 395 (1992).

[30] A. Grossmann and J. Morlet, Decomposition of Hardy functions into square integrable wavelets of constant shape, SIAM J. Math. Anal. **15**, 723 (1984).

[31] A. Grossmann, R. Kronland-Martinet, and J. Morlet, Reading and understanding continuous wavelet transforms, in *Wavelets*, edited by J.-M. Combes, A. Grossmann, and P. Tchamitchian (Springer, Berlin, 1989) pp. 2–20.

[32] C. Torrence and G. P. Compo, A practical guide to wavelet analysis, Bull. Am. Meteorol. Soc. **79**, 61 (1998).

[33] D. L. Donoho and I. M. Johnstone, Ideal spatial adaptation by wavelet shrinkage, Biometrika **81**, 425 (1994).

[34] I. M. Johnstone and B. W. Silverman, Wavelet threshold estimators for data with correlated noise, J. R. Stat. Soc. B **59**, 319 (1997).

[35] L. Barsotti, S. Gras, M. Evans, and P. Fritschel, The updated Advanced LIGO design curve, LIGO Scientific Collaboration Technical Note No. T1800044-v5, updated from T0900288-v3, 2018, doi: 10.7935/GT1W-FZ16.

[36] A. Bohé *et al.*, Improved effective-one-body model of spinning, nonprecessing binary black holes for the era of gravitational-wave astrophysics with advanced detectors, Phys. Rev. D **95**, 044028 (2017).

[37] B. Bécsy, P. Raffai, N. J. Cornish, R. Essick, J. Kanner, E. Katsavounidis, T. B. Littenberg, M. Millhouse, and S. Vitale, Parameter estimation for gravitational-wave bursts with the BayesWave pipeline, Astrophys. J. **839**, 15 (2017).

[38] J. Aasi *et al.* (LIGO Scientific Collaboration), Advanced LIGO, Class. Quantum Grav. **32**, 074001 (2015).

[39] G. M. Harry (LIGO Scientific Collaboration), Advanced LIGO: The next generation of gravitational wave detectors, Class. Quantum Grav. **27**, 084006 (2010).

[40] T. Accadia *et al.*, Virgo: A laser interferometer to detect gravitational waves, J. Instrum. **7**, P03012 (2012).

[41] F. Acernese *et al.* (VIRGO Collaboration), Advanced Virgo: A second-generation interferometric gravitational wave detector, Class. Quantum Grav. **32**, 024001 (2015).

[42] G. Pratten *et al.*, Computationally efficient models for the dominant and subdominant harmonic modes of precessing binary black holes, Phys. Rev. D **103**, 104056 (2021).

[43] I. Hinder, L. Kidder, H. Pfeiffer, M. Scheel, M. Boyle, D. Hemberger, G. Lovelace, and B. Szilagyi, Binary black-hole simulation SXS:BBH:0323 (Zenodo, 2019), doi: 10.5281/zenodo.3326442.

[44] LIGO Scientific Collaboration, LIGO Algorithm Library LAL-Suite, free software (GPL), 2018.

[45] C. Hoy and V. Raymond, Pesummary: The code agnostic parameter estimation summary page builder, SoftwareX **15**, 100765 (2021).

[46] B. P. Abbott *et al.* (LIGO Scientific Collaboration and Virgo Collaboration), A guide to LIGO–Virgo detector noise and extraction of transient gravitational-wave signals, Class. Quantum Grav. **37**, 055002 (2020).

[47] R. Abbott *et al.* (LIGO Scientific Collaboration and Virgo Collaboration), Tests of general relativity with GWTC-3, arXiv:2112.06861.

[48] M. Vallisneri, J. Kanner, R. Williams, A. Weinstein, and B. Stephens, The LIGO Open Science Center, J. Phys.: Conf. Ser. **610**, 012021 (2015).

[49] R. Abbott *et al.* (LIGO Scientific Collaboration and Virgo Collaboration), Open data from the first and second observing runs of Advanced LIGO and Advanced Virgo, SoftwareX **13**, 100658 (2021).

[50] G. Ashton *et al.*, BILBY: A user-friendly Bayesian inference library for gravitational-wave astronomy, Astrophys. J. Suppl. Ser. **241**, 27 (2019).

[51] I. M. Romero-Shaw *et al.*, Bayesian inference for compact binary coalescences with BILBY: validation and application to the first LIGO–Virgo gravitational-wave transient catalogue, Mon. Not. R. Astron. Soc. **499**, 3295 (2020).

[52] P. Schmidt, M. Hannam, and S. Husa, Towards models of gravitational waveforms from generic binaries: A simple approximate mapping between precessing and non-precessing inspiral signals, Phys. Rev. D **86**, 104063 (2012).

[53] M. Hannam, P. Schmidt, A. Bohé, L. Haegel, S. Husa, F. Ohme, G. Pratten, and M. Pürrer, Simple Model of Complete Precessing Black-Hole-Binary Gravitational Waveforms, Phys. Rev. Lett. **113**, 151101 (2014).

[54] T. B. Littenberg and N. J. Cornish, Bayesian inference for spectral estimation of gravitational wave detector noise, Phys. Rev. D **91**, 084034 (2015).

[55] B. P. Abbott *et al.* (LIGO Scientific Collaboration and Virgo Collaboration), GW151226: Observation of Gravitational Waves from a 22-Solar-Mass Binary Black Hole Coalescence, Phys. Rev. Lett. **116**, 241103 (2016).

[56] B. P. Abbott *et al.* (LIGO Scientific Collaboration and Virgo Collaboration), Binary Black Hole Mergers in the First Advanced LIGO Observing Run, Phys. Rev. X **6**, 041015 (2016); **8**, 039903 (2018).

[57] B. P. Abbott *et al.* (LIGO Scientific Collaboration and Virgo Collaboration), GW170104: Observation of a 50-Solar-Mass Binary Black Hole Coalescence at Redshift 0.2, Phys. Rev. Lett. **118**, 221101 (2017); **121**, 129901 (2018).

[58] B. P. Abbott *et al.* (LIGO Scientific Collaboration and Virgo Collaboration), GW170608: Observation of a 19-solar-mass binary black hole coalescence, Astrophys. J. **851**, L35 (2017).

[59] B. P. Abbott *et al.* (LIGO Scientific Collaboration and Virgo Collaboration), GW170814: A Three-Detector Observation of Gravitational Waves from a Binary Black Hole Coalescence, Phys. Rev. Lett. **119**, 141101 (2017).

[60] K. Chatziioannou *et al.*, On the pProperties of the massive binary black hole merger GW170729, Phys. Rev. D **100**, 104015 (2019).